CRPropa: A Numerical Tool for the Propagation of UHE Cosmic Rays, $\gamma-$rays and Neutrinos

Eric Armengaud[a,b]**, Günter Sigl**[a,b]**, Tristan Beau**[a]**,**
Francesco Miniati[c]

[a]APC ‡ (AstroParticule et Cosmologie), 11, place Marcelin Berthelot, F-75251 Paris
Cedex 05, France
[b] GReCO, Institut d'Astrophysique de Paris, C.N.R.S., 98 bis boulevard Arago,
F-75014 Paris, France
[c] Physics Department, ETH Zürich, 8093 Zürich, Switzerland

E-mail: `armengau@in2p3.fr`

Abstract. To understand the origin of ultra-high energy cosmic rays (UHECRs, defined to be above 10^{18} eV), it is required to model in a realistic way their propagation in the Universe. UHECRs can interact with low energy radio, microwave, infrared and optical photons to produce electron/positron pairs or pions. The latter decay and give rise to neutrinos and electromagnetic cascades extending down to MeV energies. In addition, deflections in cosmic magnetic fields can influence the spectrum and sky distribution of primary cosmic rays and, due to the increased propagation path length, the secondary neutrino and $\gamma-$ray fluxes. Neutrino, $\gamma-$ray, cosmic ray physics and extra-galactic magnetic fields are, therefore, strongly linked subjects and should be considered together in order to extract maximal information from existing and future data, like the one expected from the Auger Observatory. For that purpose, we have developed CRPropa, a publicly-available numerical package which takes into account interactions and deflections of primary UHECRs as well as propagation of secondary electromagnetic cascades and neutrinos. CRPropa allows to compute the observable properties of UHECRs and their secondaries in a variety of models for the sources and propagation of these particles. Here we present physical processes taken into account as well as benchmark examples; a detailed documentation of the code can be found on our web site.

PACS numbers: 98.70.Sa, 13.85.Tp, 98.65.Dx, 98.54.Cm

1. Introduction

Astroparticle physics is currently experimentally driven and involves many different existing or planned projects ranging from UHECR observatories such as the Pierre Auger Observatory [1], to neutrino telescopes [2], as well as ground and space based $\gamma-$ray detectors operating at TeV and GeV energies, respectively [3]. It is clear that GeV-TeV $\gamma-$ray and neutrino astronomy will prove an invaluable tool to unveil the sources, and probe into the mechanism, of UHECRs. Even if a putative source were to produce exclusively UHECRs, photo-pion [4] and pair production by protons on the cosmic microwave background (CMB) would lead to guaranteed secondary photon and neutrino fluxes that could be detectable. Furthermore, spectra, power and sky distributions of both primary UHECRs and secondary $\gamma-$rays and neutrinos depend on the poorly known large scale cosmic magnetic fields.

It is, therefore, desirable to have a general numerical tool that can treat the interface between UHECR, $\gamma-$ray and neutrino astrophysics, and large scale magnetic fields. To this end, we have recently merged our Monte Carlo code for simulating deflections of UHECRs in a structured, magnetized Universe [5] with a one-dimensional transport code that solves electromagnetic (EM) cascades and neutrino propagation [6]. With the present paper, we release a public version of this unified code which we hope could be useful for the whole community.

In the following, we present the relevant interactions and propagation phenomena taken into account, and the propagation algorithms applied in CRPropa. We also present a few examples of how to use the code in practice. The numerical package and its detailed documentation are available for downloading on the CRPropa website, `http://apcauger.in2p3.fr/CRPropa`.

We use natural units, $c = \hbar = 1$ throughout this paper.

2. Propagation algorithms

UHECRs are injected at specified sources, and propagated step-by-step in either a one- or a three-dimensional environment. The trajectories are regularly sampled, or recorded only at specific locations (e.g. at a given distance from a source, or at an "observer" point). Each propagation step consists in integrating the Lorentz equations, and computing the interactions and possibly the secondaries generated by those interactions.

In the 3-dimensionnal case, a "simulation box" is defined and periodic boundary conditions are assumed.

When deflections are taken into account, cosmological redshifts cannot be computed, because the propagation time until the particle reaches the observer is not known before hand. Therefore, redshift evolution is only accounted for in the 1D version of the package. The concordance cosmology is used for which, assuming a flat Universe, the Hubble rate $H(z)$ at redshift z in the matter dominated regime, $z \lesssim 10^3$, is given
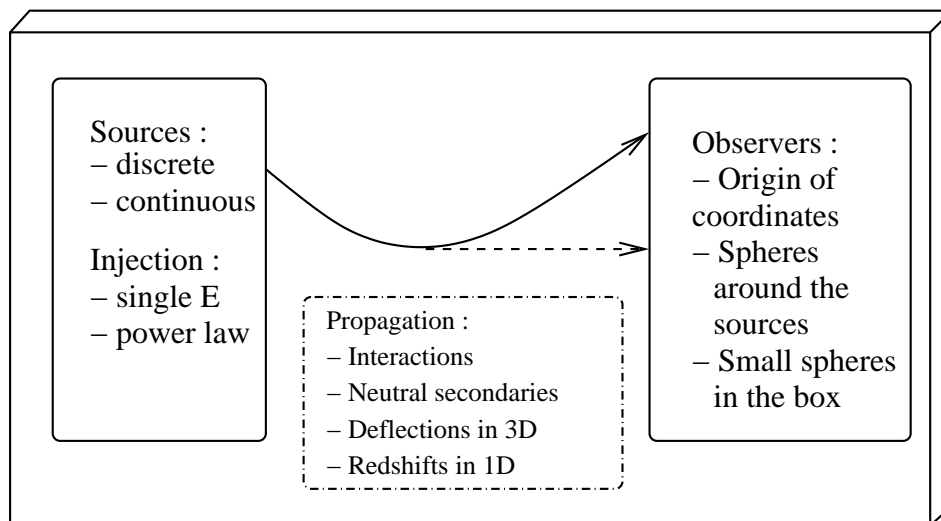
Figure 1. Principle of the propagation algorithm. This scheme applies to all configurations.

by

$$H(z) = H_0 \left[\Omega_{\mathrm{m}}(1+z)^3 + \Omega_\Lambda \right]^{1/2} . \tag{1}$$

The parameters Ω_{m} and Ω_Λ can be freely chosen, their standard values being $\Omega_{\mathrm{m}} = 0.3$, $\Omega_\Lambda = 0.7$, and $H_0 = h_0\,100$ km s^{-1} Mpc^{-1} with $h_0 = 0.72$.

The general principle of the simulations is shown in Fig. 1.

2.1. Nucleon Interactions

The most famous interaction of nucleons with the low-energy photon backgrounds is pion production, which generates the GZK feature. In order to handle pion production, we use the event generator SOPHIA [7], that has been explicitly designed to study this phenomenon and that uses the particle production cross-sections measured in accelerators. We have also augmented the SOPHIA package for interactions with a low energy extragalactic background light (EBL) with a general energy distribution. SOPHIA allows to determine the distribution of the stables particles generated by an interaction with a low-energy photon.

Pair production by protons (PPP) on the CMB, also known as Bethe-Heitler process, is taken into account as a continuous energy loss whose rate we evaluate following the expressions in Refs. [8, 9]. For the spectrum of the pairs we exploit the fact that Bethe-Heitler and triplet pair production, $e\gamma_b \rightarrow ee^+e^-$, are analogous electromagnetic processes, their cross sections and inelasticities converging for relativistic pairs. Fig. 2 of Ref. [10] then shows that the spectrum of electron-positron pairs (heretoafter simply referred to as electrons) generated by a proton of energy E can be approximated by a power-law energy distribution $dn/dE_e \propto E_e^{-7/4}$. Kinematics implies that this power law holds for $E_{\mathrm{min}} \leq E_e \leq E_{\mathrm{PPP}}$, where the minimal

and maximal energies are given by [6]

$$E_{\text{PPP}} \simeq \frac{4E^2\varepsilon}{4E\varepsilon + m_p^2} \simeq \frac{4.5 \times 10^{15} \left(\frac{E}{\text{EeV}}\right)^2 \left(\frac{\varepsilon}{\text{meV}}\right) \text{ eV}}{4.6 \times 10^{-3} \left(\frac{E}{\text{EeV}}\right) \left(\frac{\varepsilon}{\text{meV}}\right) + 1}$$

$$E_{\text{min}} \simeq \frac{m_e^2}{8\varepsilon} \simeq 3.3 \times 10^{13} \left(\frac{\varepsilon}{\text{meV}}\right)^{-1} \text{ eV} . \tag{2}$$

In Eq. (2), m_p and m_e are the proton and electron masses, respectively, ε is the low energy target photon energy, and the approximation for E_{min} holds for $m_e m_p \lesssim 4E\varepsilon \lesssim m_p^2$. The average electron energy is then $\overline{E_e} = \int_{E_{\text{min}}}^{E_{\text{PPP}}} dE_e E_e E_e^{-7/4} / \int_{E_{\text{min}}}^{E_{\text{PPP}}} dE_e E_e^{-7/4} \simeq 3 E_{\text{min}}^{3/4} E_{\text{PPP}}^{1/4}$ which is indeed much smaller than the primary proton energy E. From Eq. (2), the inelasticity $K \equiv \overline{E_e}/E$, whose precise energy dependence can be found in Ref. [9], for $m_e m_p \lesssim 4E\varepsilon \lesssim m_p^2$ can thus be approximated by

$$K(E\varepsilon) \sim \frac{3}{2^{7/4}} \frac{m_e^{3/2}}{(E\varepsilon\, m_p)^{1/2}} \tag{3}$$

$$\simeq 3.4 \times 10^{-4} \left(\frac{E}{\text{EeV}}\right)^{-1/2} \left(\frac{\varepsilon}{\text{meV}}\right)^{-1/2} ,$$

This is consistent with Figs. 1 and 2 in Ref. [11]. For our purposes, we are not sensitive to the lower kinematic limit since the total energy produced $\propto \int_{E_{\text{min}}}^{E_{\text{PPP}}} dE_e E_e E_e^{-7/4} \simeq 4E_{\text{PPP}}^{1/4}$ is insensitive to E_{min} as long as $E_{\text{min}} \ll E_{\text{PPP}}$, but rather is dominated by the highest energies. As a consequence, the total proton energy loss rate due to pair production is dominated by the highest energy electrons close to E_{PPP}. However, because the production cross section of these highest energy electrons is much smaller than the one for the more numerous lower energy electrons, the average inelasticity Eq. (3) is nevertheless small, below 10^{-3} everywhere above the pair production threshold. The spectrum and maximal energy of the pairs will be important for the synchrotron spectrum emitted by these electrons in an EGMF of strength B which peaks at $\simeq 6.8 \times 10^{11} \left(E_e/10^{19}\,\text{eV}\right)^2 (B/0.1\,\mu\text{G})\,\text{eV}$.

Nucleons can be followed down to $10^{17}\,\text{eV}$ with CRPropa, below which interactions become negligible.

2.2. Secondary Electromagnetic Cascades and Neutrinos

The secondary neutrinos from pion production of nucleons are propagated in straight lines assuming no energy losses except redshift effects.

All the EM products of these interactions are evolved using an EM cascade code based on Ref. [6]. The photons and pairs are followed until either their energy drops below 100 MeV or they reach an observer. All relevant interactions with a background photon γ_b are taken into account, namely single pair production (PP), $\gamma\gamma_b \to e^+e^-$, double pair production (DPP), $\gamma\gamma_b \to e^+e^-e^+e^-$, inverse Compton scattering (ICS), $e\gamma_b \to e\gamma$, and triplet pair production (TPP), $e\gamma_b \to ee^+e^-$ (see also Ref. [12] for a detailed discussion of implemented interactions). In addition, synchrotron losses of electrons in the (in general) inhomogeneous EGMF are taken into account and the

resulting lower energy synchrotron photons are also followed in the subsequent EM cascade.

This module has been applied to EM cascades from discrete magnetized proton sources in galaxy clusters in Ref. [13]. A semi-analytical discussion of photon production by cosmic rays in the magnetic field environment of galaxy clusters has been given in Ref. [14].

The EM cascades that are followed with the current version of CRPropa are propagated in straight lines, even in the case of 3-dimensionnal simulations for UHECRs: Every time a primary hadron interacts and initiates an EM cascade, it is assumed that the secondaries propagate along straight lines and it is checked whether the line of sight crosses the observer. If this is the case, the EM cascade module is called with the corresponding propagation distance and the projected magnetic field profile. Electrons in the EM cascade can of course be deflected in the EGMF, and we discuss here under which circumstances these deflections can be neglected.

In a magnetic field of strength B the synchrotron cooling time for an electron of energy E_e is given by

$$t_{\text{synch}} = \frac{E_e}{dE_e/dt} = \frac{6\pi m_e^2}{\sigma_T E_e B^2}$$

$$\simeq 3.84 \, \text{kpc} \left(\frac{E_e}{10^{15} \, \text{eV}}\right)^{-1} \left(\frac{B}{\mu \, \text{G}}\right)^{-2},$$

(4)

where σ_T is the Thomson cross section. The inverse Compton energy loss length is [12]

$$t_{\text{IC}} \lesssim 500 \, \text{pc} \left(\frac{E_e}{10^{15} \, \text{eV}}\right) \quad \text{for } E_e \gtrsim 10^{15} \, \text{eV}.$$

(5)

Approximate equality holds for $E_e \gtrsim 10^{18} \, \text{eV}$ in Eq. (5) if the universal radio background is negligible. More realistically, at these energies the energy loss length is between a factor ~ 30 and a few hundred smaller than the numerical value in Eq. (5). For $E_e \lesssim 10^{15} \, \text{eV}$, ICS is dominated by the CMB, with a cross section approaching the Thomson cross section, such that

$$t_{\text{IC}} \lesssim 1.2 \, \text{kpc} \quad \text{for } E_e \lesssim 10^{15} \, \text{eV}.$$

(6)

These length scales as well as the maximal propagation distance have to be compared with the Larmor radius

$$r_L = \frac{E_e}{eB} \simeq 1.08 \, \text{pc} \left(\frac{E_e}{10^{15} \, \text{eV}}\right) \left(\frac{B}{\mu \, \text{G}}\right)^{-1}.$$

(7)

In order for a one-dimensional treatment of EM cascades to be valid, the Larmor radius has to be much larger than either the total propagation length, the IC or the synchrotron loss lengths. From Eqs. (5) and (7) we see that this is certainly the case for $B \lesssim 1 \, \text{nG}$ and $E_e \gtrsim 10^{15} \, \text{eV}$ because the energy loss length against IC is smaller than the Larmor radius. From Eqs. (6) and (7), it is also the case for $B \lesssim 10^{-12} \, \text{G}$ and $E_e \gtrsim 1 \, \text{TeV}$. Comparing Eqs. (4) and (7) shows that the conditions are also met
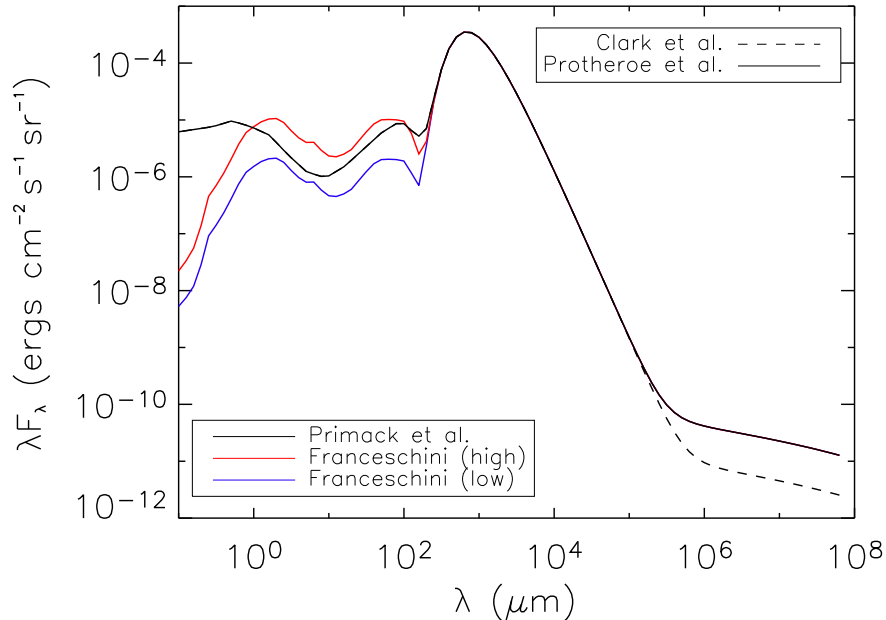
Figure 2. Models implemented for the low energy photon background at zero redshift. The IRB consists basically of a peak in the far infrared around 100μ m dominated by dust and a peak in the near infrared dominated by stars.

for $B \gtrsim 1\,\mathrm{nG}$ and $E_e \gtrsim 10^{18}\,\mathrm{eV}$ where synchrotron loss degrades electron energies over scales smaller than the Larmor radius.

In contrast, these conditions are not met for $E_e \lesssim 10^{15}\,\mathrm{eV}$ and $B \gtrsim 10^{-12}\,\mathrm{G}$ because deflection becomes large for propagation over more than a few Mpc and synchrotron and IC are negligible. However, electrons at energies $E_e \lesssim 10^{15}\,\mathrm{eV}$, in general do not significantly contribute to γ−ray fluxes above a MeV we are interested in.

The 1D approximation of EM cascades adopted in this code is, therefore, in general met if the low energy part of the cascades develops mostly in voids where the EGMF is negligible, whereas the high energy part develops in structures with fields above $\sim 1\,\mathrm{nG}$. If sources follow the large scale structure and are considerably magnetized, this is in general the case.

2.3. Background Photon Spectra and their Evolution

Fig. 2 shows the EBL energy distributions that have been implemented. The most important is the CMB. For the infrared background (IRB) we implemented three distributions, a low and a high version of Franceschini et al. [15] which differ roughly by a factor 5, as well as the one by Primack et al. [16]. The low Franceschini et al. and the Primack et al. backgrounds are consistent with recent upper limits from blazar observations in TeV γ−rays by HESS [17]. For a recent review of the IRB see for

example Ref. [18].

The IRB has a significant influence on EM cascades only around the threshold for pair production, i.e. between a few Tev and $\simeq 100\,\text{TeV}$. At higher energies, the $\gamma-$ray flux is suppressed by interactions with the CMB and, above $\simeq 10^{19}\,\text{eV}$, by interactions with with the radio background. At energies below $\sim \text{TeV}$, the Universe acts as a calorimeter and the total photon flux is proportional to the total EM energy injected above $\sim \text{PeV}$ with a rather universal shape [19].

Although its photon number density $\simeq 2\,\text{cm}^{-3}$ is a factor $\simeq 200$ smaller than for the CMB, below the GZK-cutoff and above $\sim 10^{17}\,\text{eV}$ the IRB can significantly reduce the nucleon mean free path for pion production. This can be important for secondary photon and neutrino [20, 21] production, especially for a steep primary injection spectrum and/or strong redshift evolution.

For the universal radio background (URB) we use a weak and a strong version based on Ref. [22] and on observations [23]. The URB is mostly important for EM cascades above $\sim 10^{18}\,\text{eV}$ where it can inhibit cascade development due to the resulting small pair production lengths, especially for fast synchrotron losses of electrons in the presence of strong magnetic fields.

Since URB photons can give rise to pion production only above a few times $10^{22}\,\text{eV}$, where the interaction rate is essentially proportional to the total EBL photon density which is dominated by the CMB by a factor $\sim 10^3$, see Fig. 2, the URB is negligible for pion production. The same applies to pair production by protons.

Figs. 3 and 4 show interaction and energy loss lengths for protons and interaction lengths of photons, respectively, and their dependence on EBL models at zero redshift. This demonstrates that the IRB becomes important for pion production by protons below the GZK cutoff and for pair production by photons below the threshold in the CMB at $\sim 10^{14}\,\textbf{eV}$. It also shows that the URB tends to dominate pair production by photons above $\sim 10^{19}\,\text{eV}$.

The redshift evolution of the cosmic microwave background (CMB) is trivial. The redshift evolution of the radio and infrared distributions is more complicated: Ultra-relativistic particles of energy E injected at redshift z' with a rate per energy and comoving volume $\Phi(E, z')$ result in a *physical* number density per energy at redshift z given by

$$n(E, z) = (1+z)^3 \int_z^\infty dz' \frac{4\pi\Phi\left[E_i(E, z, z'), z'\right]}{(1+z')H(z')}$$
$$\times \frac{dE_i}{dE}(E, z, z'), \tag{8}$$

where it is assumed that the particle looses energy continuously such that its injection energy can be computed analytically, $E_i(E, z, z')$. Interactions of the low energy EBL photons, whose differential number densities we will denote by $n_b(\varepsilon, z)$ in the following to distinguish from the high energy particles, can safely be neglected after recombination,
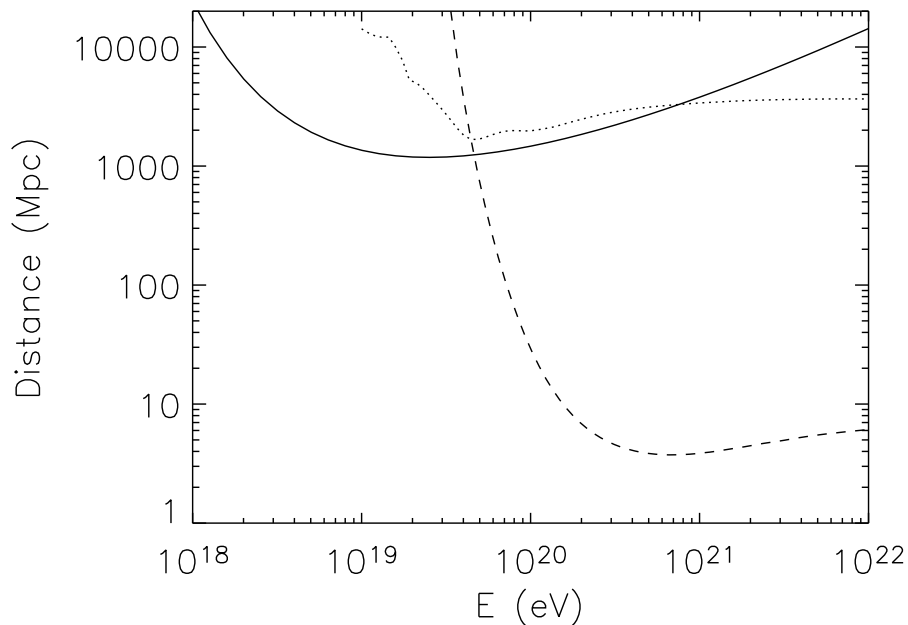
Figure 3. Proton energy loss length for pair production on the CMB (continuous line), interaction length for pion production on the CMB (dashed line) and on the Primack et al. IRB (dotted line) at $z = 0$. The irregularities in the dashed curve are due to the piecewise power law fits of the Primack et al. IRB.

$z \lesssim 10^3$, such that $E_i(E, z, z') = (1 + z')E/(1 + z)$. Eq. (8) then simplifies to

$$n_b(\varepsilon, z) = (1 + z)^2 \int_z^\infty dz' \frac{4\pi\Phi\left[(1 + z')\varepsilon/(1 + z), z'\right]}{H(z')} , \tag{9}$$

By using $|dt/dz| = [(1 + z)H(z)]^{-1}$, one can see easily that the total energy density per comoving volume redshifts as $\int d\varepsilon\, \varepsilon\, n_b(\varepsilon, z)/(1 + z)^3 = (1 + z) \int dt\, d\varepsilon_i\, \Phi(\varepsilon_i, z')/(1 + z')$, as it should be.

For the URB we implemented a nontrivial redshift evolution in the cascade module, as this can be relevant for EM cascade development. We assume that $\Phi_{\mathrm{URB}}(\varepsilon, z) = \phi_{\mathrm{URB}}(\varepsilon)g_{\mathrm{URB}}(z)$ factorizes into an energy dependence $\phi_{\mathrm{URB}}(\varepsilon)$ motivated by the observations [23] and theoretical estimates [22] and a redshift dependence given by
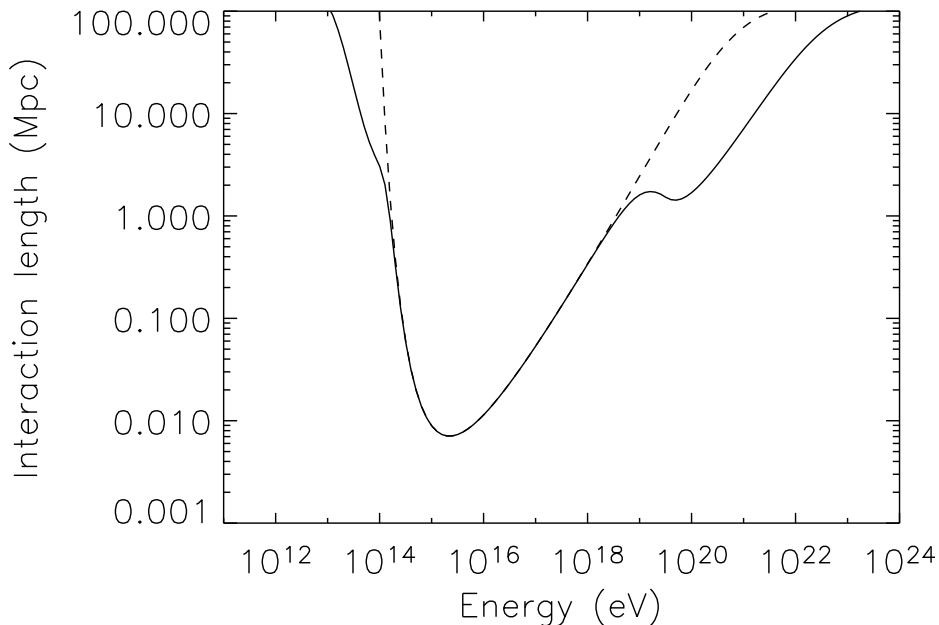
$$g_{\mathrm{URB}}(z) = 10^{1.18z - 0.28z^2} , \tag{10}$$

as in Ref. [6].

For the Primack et al. IRB [16] we use for simplicity the differential photon energy distribution evolution

$$n_b(\varepsilon, z) = \left\{ \begin{array}{ll} (1 + z)^2 n_b\left(\frac{\varepsilon}{1+z}, z = 0\right) & \text{for } z \le z_b , \\ 0 & \text{otherwise} \end{array} \right\} \tag{11}$$

Figure 4. Photon interaction length at $z = 0$ on the EBL consisting of the CMB, the Primack et al. IRB, and the strong URB version. Dotted line: Interaction length in the CMB only at $z = 0$.

which corresponds to instantaneous creation of the background at redshift z_b with $\Phi(\varepsilon, z') = H(z_b)n_b[\varepsilon/(1 + z_b), z = 0]\delta(z' - z_b)/(4\pi)$ in Eq. (9). It strictly applies to the CMB which was effectively produced at decoupling, $z_b \sim 1100$. For the IRB we assume $z_b = 5$. Interaction lengths $l(E, z)$ and, in case of continuous energy loss processes such as PPP, energy loss rates $b(E, z) \equiv dE/dt$ then follow simple scaling relations in redshift [21],

$$l(E, z)^{-1} = (1 + z)^3 l\left[(1 + z)E, z = 0\right]^{-1}$$
$$b(E, z) \;\; = (1 + z)^2 b\left[(1 + z)E, z = 0\right] . \tag{12}$$

This simplifies implementation in SOPHIA.

2.4. Distributions and Properties of Sources

Both single sources and realizations of both discrete or continuous source distributions can be used in CRPropa. In the latter case, the distributions can be selected, for example, to follow the baryon density from a large scale structure simulation box, and are periodically repeated.

The UHECR particles are injected isotropically around the sources with a monochromatic or a power-law energy distribution between a minimal and a maximal energy, $E_{\min}$ and $E_{\max}$, respectively:

$$\frac{dN}{dE_{\mathrm{inj}}} \propto E_{\mathrm{inj}}^{-\alpha} \qquad E_{\mathrm{min}} \leq E_{\mathrm{inj}} \leq E_{\mathrm{max}}$$

For each trajectory reaching the observer and being registered, the source identity i is also registered. This allows to apply a re-weighting procedure on the recorded "events", in order to vary individual source properties such as their injection power law index α_i or luminosity Q_i. For example, it is most efficient in terms of CPU time to inject the UHECRs with a spectral index $\alpha_0 = 1$ at the sources, that is with a uniform distribution in the logarithm of the energy. By re-weighting each recorded event by a factor $w \propto Q_i E_{\mathrm{inj}}^{\alpha_i - 1}$, the source i would contribute with a power Q_i and an effective injection power law index α_i in all observables constructed from the weighted trajectory sample.

## 3. Large Scale Structure and Magnetic Fields

The strength and distribution of the EGMF is currently poorly known and their impact on UHECR are hard to quantify, as demonstrated by the different results in Refs. [5, 24]. See also Ref. [25] for a discussion of these differences and Ref. [26] for a review on EGMF. We note that there are recent observational hints of EGMF as strong as $\sim 0.1\mu\,$G on scales as extended as superclusters [27], as well as theoretical motivations for such fields [28].

Enhanced magnetic fields around large scale structures such as galaxy clusters together with associated larger EBL densities can lead to increased production of $\gamma-$rays and neutrinos.

The EGMF from the large scale structure simulation from Ref. [29, 30] has so far been implemented in CRPropa, but any magnetic field model can be used. Within the public package CRPropa, only a small subgrid of the simulations from [29, 30] is provided in order to allow simple tests.

Fig. 5 shows a 2D cross section through the environment of a galaxy cluster from this simulation.

Large scale structure simulations usually cover only a small fraction of today's Universe, typically of order 100 Mpc in linear scale. Since sources at much larger, cosmological distances can contribute to the fluxes of UHECR below the GZK cutoff, of photons below $\sim$ TeV and of neutrinos, the EGMF and source distributions are periodically continued in the 3D version of the code. EGMF with homogeneous statistical properties and power law spectra in Fourier space (e.g. a Kolmogorov spectrum) have also been implemented in the package.
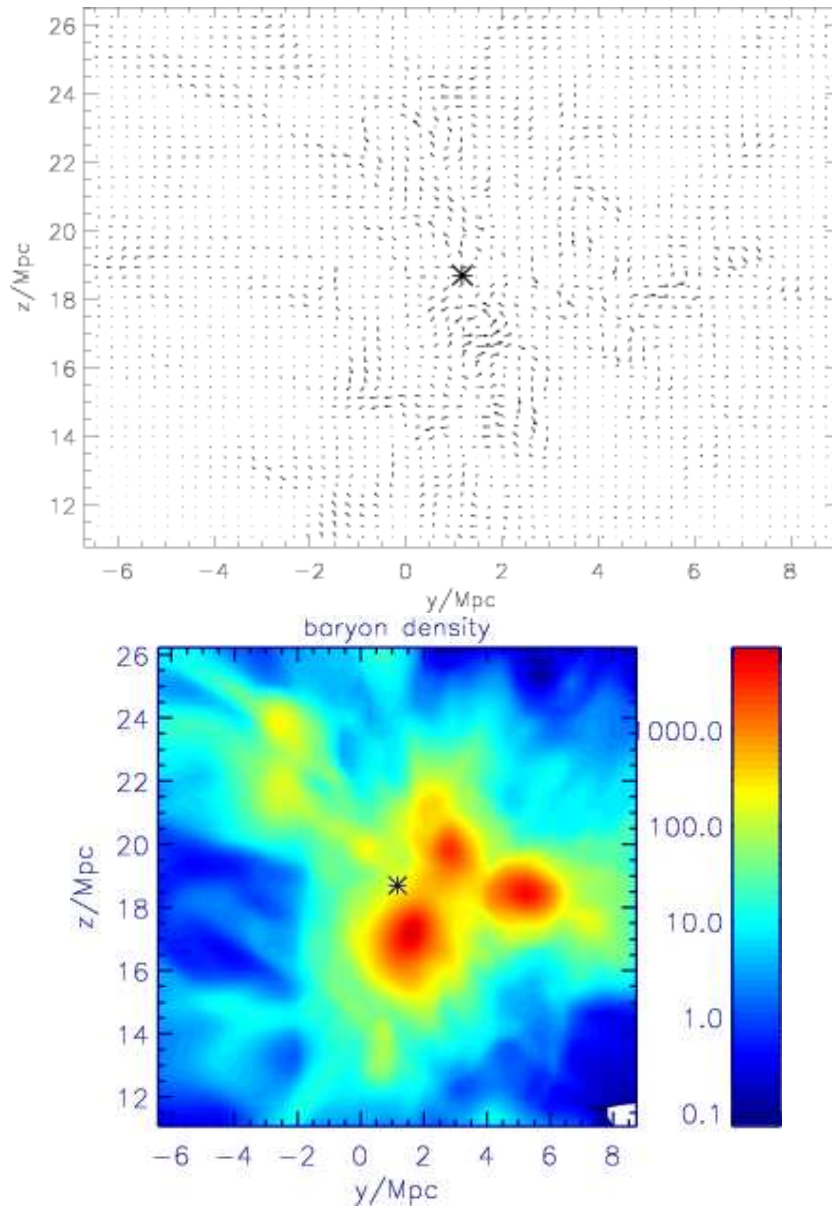
Figure 5. A 2D cross section through the relative size and polarization of the EGMF in linear scaling, (top panel) and the relative baryon density in logarithmic scaling (bottom panel) in the environment of a galaxy cluster from the simulations from Ref. [29, 30].
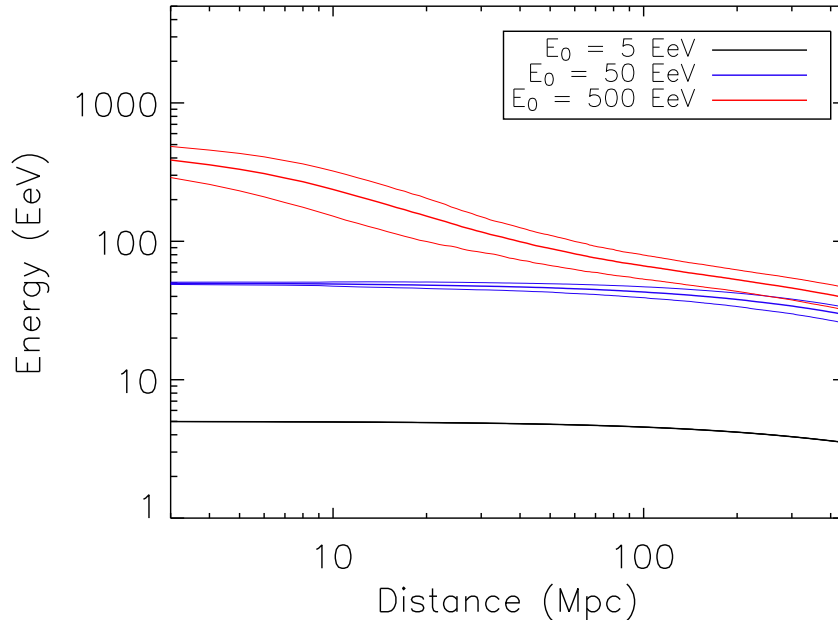
Figure 6. Evolution of the energy of nucleons as a function of propagation distance, for initial energies of 5, 50 or 500 EeV. The thin lines indicate the dispersion induced by the stochasticity of pion production.

4. Sample Applications

We present here applications of CRPropa that are obtained with very simple configurations requiring little CPU time. The results can easily be compared with previous results from the literature.

Fig. 6 shows the averages and dispersions of the energy of nucleons in a one-dimensional simulation, as a function of propagated distance for various initial energies. Using SOPHIA automatically enables us to reproduce the stochasticity of pion production.

Fig. 7 shows the spectra of secondaries generated during the one-dimensional propagation of UHECRs from a source located at 20 Mpc or 100 Mpc from the observer. Note that the neutrino flux increases with distance to the source, whereas the photon flux above $\sim 10^{14}$ eV decreases, but the photon flux below this energy increases. This is because more secondary neutrinos and EM particles are produced for larger propagation distances, but EM particles above $\sim 10^{14}$ eV are quickly degraded and cascade down to sub-PeV energies. A more detailed analysis of the fluxes of secondaries from a single UHECR source can be found in Ref. [13].

Fig. 8 shows the spectra of secondary neutrinos from a source located at 20 Mpc from an observer, depending in particular on the magnetic field effects. It is remarkable that, for a given source luminosity, the flux of secondary neutrinos is increased by a
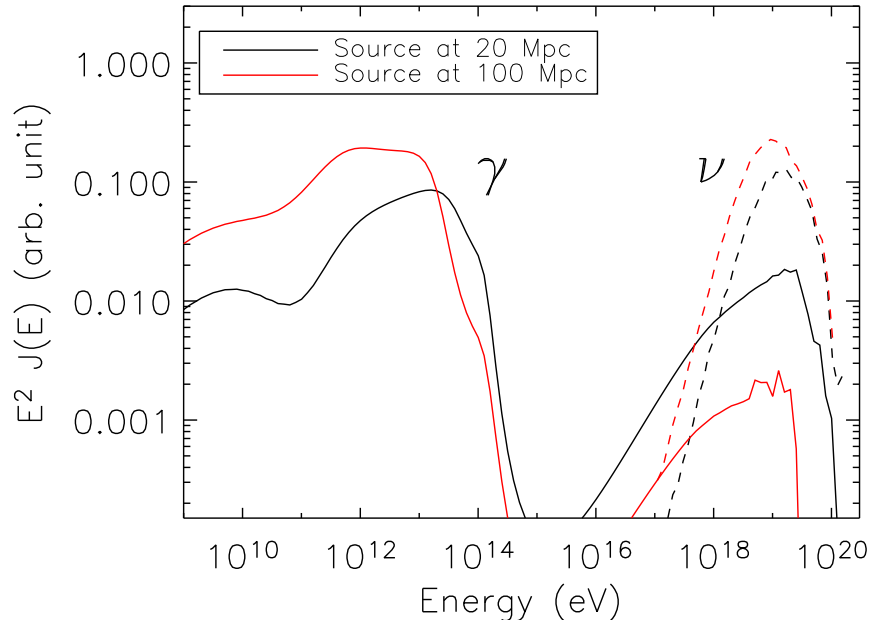
Figure 7. Spectrum of secondary photons and neutrinos generated by pion and pair production from a single UHECR source at a given distance. We consider here a one-dimensionnal model, with an injection spectral index $\alpha = 2$ for the UHECRs. A uniform magnetic field of 0.1 nG is assumed. The fluctuations at the highest energies are statistical.

factor of more than two due to the enhancement of the UHECR propagation distance generated by the μG-level magnetic fields that surround this source.

Fig. 9 compares the spectral shape of UHECRs from a source located at 100 Mpc from an observer, depending on the presence of magnetic fields around the source. If magnetic fields of amplitude $\sim \mu G$ surround the source over a few Mpc, the observed spectrum is clearly modified: 1) there is a dispersion in the true propagation distance, compared to a fixed propagation distance of 100 Mpc. This reduces the amplitude of the "bump"; 2) the mean propagation distance is increased compared to 100 Mpc. This leads to a GZK cut-off at slightly lower energies.

5. Conclusions

We have presented the first public package to study systematically the properties of the propagation of UHECRs and their secondaries in a structured magnetized Universe. We have detailed the interactions that are already implemented, and presented a few simple examples obtained directly by running the CRPropa code.

A major advantage of CRPropa is its large modularity, which should allow various users to implement their own modules, adapted to specific UHECR propagation models.
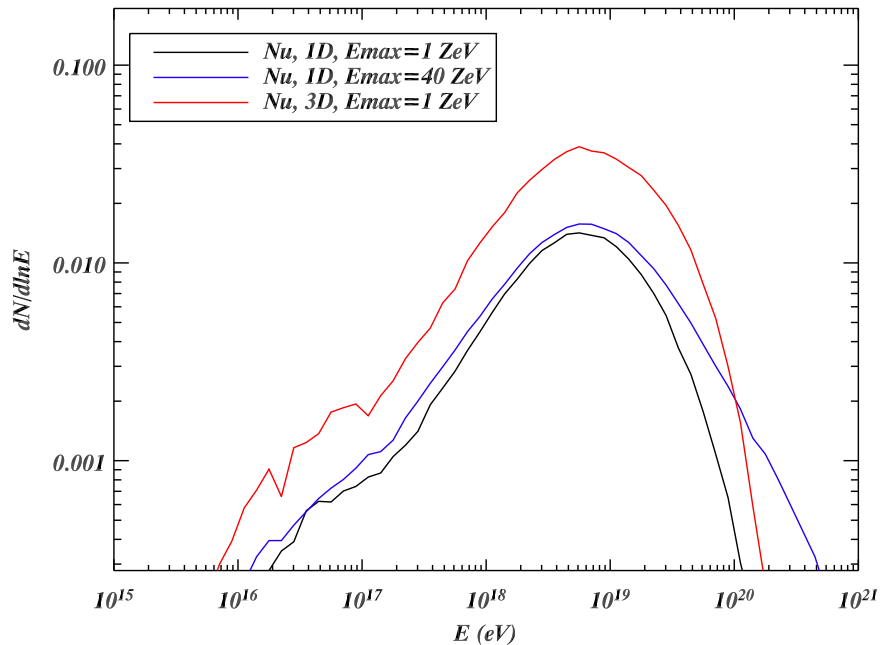
Figure 8. Secondary neutrinos from a nearby source of UHECRs with a given luminosity. The flux increases at high energies both with maximum UHECR acceleration energy and with the strength of magnetic fields surrounding the source. The fluctuations at low energy are statistical.

Many possible upgrades of the CRPropa package can be considered: This includes the implementation of non-uniform grids for magnetic field models, of UHE nuclei and secondary neutrinos and EM particles from their interactions, of inhomogeneous low energy target photon backgrounds for the UHE nuclei and EM cascade interactions, and of hadronic interactions with the baryon gas in dense parts of the large scale structure. Finally, interactions of UHE neutrinos with relic neutrinos of arbitrary mass and clustering properties could also be implemented, including the resulting secondary particles.

Acknowledgments
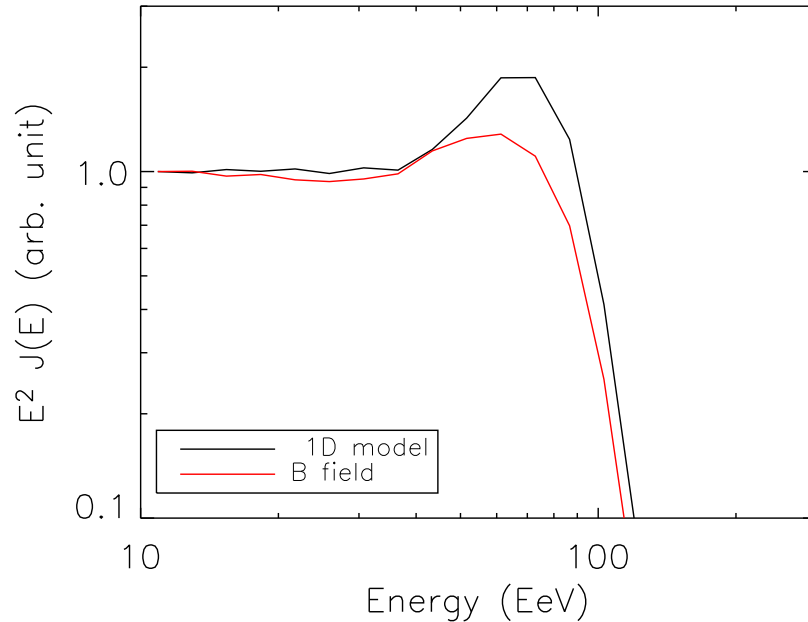
Figure 9. UHECR spectrum from a source located at 100 Mpc from an observer, with a spectral index $\alpha = 2$ and $E_{\max} = 10^{21}$ eV. The red curve is obtained from a full 3-dimensional simulation, where the source is embedded in a region with μG fields over a few Mpc.

References

[1] J. W. Cronin, Nucl. Phys. B (Proc. Suppl.) **28B** (1992) 213; The Pierre Auger Observatory Design Report (ed. 2), March 1997; see also http://www.auger.org.

[2] for recent reviews see, e.g., F. Halzen and D. Hooper, Rept. Prog. Phys. **65**, 1025 (2002) A. B. McDonald, C. Spiering, S. Schonert, E. T. Kearns and T. Kajita, Rev. Sci. Instrum. **75**, 293 (2004)

[3] for recent short reviews see, e.g., H. J. Völk, astro-ph/0401122; H. J. Völk, astro-ph/0312585.

[4] K. Greisen, Phys. Rev. Lett. **16**, 748 (1966); G. T. Zatsepin and V. A. Kuzmin, JETP Lett. **4**, 78 (1966) [Pisma Zh. Eksp. Teor. Fiz. **4**, 114 (1966)].

[5] G. Sigl, F. Miniati and T. A. Ensslin, Phys. Rev. D **70**, 043007 (2004) astro-ph/0401084.

[6] S. Lee, Phys. Rev. D **58**, 043004 (1998) astro-ph/9604098.

[7] A. Mucke, R. Engel, J. P. Rachen, R. J. Protheroe and T. Stanev, Comput. Phys. Commun. **124**, 290 (2000)

[8] G. R. Blumenthal, Phys. Rev. D **1**, 1596 (1970).

[9] M. J. Chodorowski, A. .A. Zdziarski, M. Sikora, Astrophys. J. **400**, 181 (1992).

[10] A. Mastichiadis, Mon. Not. Roy. Astron. Soc. **253**, 235 (1991).

[11] A. Mastichiadis, R. J. Protheroe and J. G. Kirk, Astron. Astrophys. **433**, 765 (2005) astro-ph/0501156.

[12] for a review see, e.g., P. Bhattacharjee and G. Sigl, Phys. Rept. **327**, 109 (2000) astro-ph/9811011.

[13] E. Armengaud, G. Sigl and F. Miniati, astro-ph/0511277.

[14] F. A. Aharonian, Mon. Not. Roy. Astron. Soc. **332**, 215 (2002).

[15] A. Franceschini, H. Aussel, C. J. Cesarsky, D. Elbaz and D. Fadda, Astron. Astrophys. **378**, 1 (2001).

[16] see, e.g., J. R. Primack, J. S. Bullock and R. S. Somerville, AIP Conf. Proc. **745**, 23 (2005) `astro-ph/0502177`.

[17] F. Aharonian *et al.* [H.E.S.S. Collaboration], `astro-ph/0508073`.

[18] G. Lagache, J. L. Puget and H. Dole, `astro-ph/0507298`.

[19] P. S. Coppi and F. A. Aharonian, Astrophys. J. **487**, L9 (1997) `astro-ph/9610176`.

[20] T. Stanev, Phys. Lett. B **595**, 50 (2004) `astro-ph/0404535`.

[21] E. V. Bugaev, A. Misaki and K. Mitsui, Astropart. Phys. **24**, 345 (2005) `astro-ph/0405109`.

[22] R. J. Protheroe and P. L. Biermann, Astropart. Phys. **6**, 45 (1996) [Erratum-ibid. **7**, 181 (1997)] `astro-ph/9605119`.

[23] T. A. Clark, L. W. Brown and J. K. Alexander, Nature **228**, 847 (1970).

[24] K. Dolag, D. Grasso, V. Springel and I. Tkachev, JETP Lett. **79**, 583 (2004) [Pisma Zh. Eksp. Teor. Fiz. **79**, 719 (2004)] `astro-ph/0310902`; K. Dolag, D. Grasso, V. Springel and I. Tkachev, JCAP **0501**, 009 (2005) `astro-ph/0410419`.

[25] G. Sigl, F. Miniati and T. Ensslin, Nucl. Phys. Proc. Suppl. **136**, 224 (2004) `astro-ph/0409098`.

[26] P. P. Kronberg, Reports of Progress in Physics 58 (1994) 325; J. P. Vallée, Fundamentals of Cosmic Physics, Vol. 19 (1997) 1; T. E. Clarke, P. P. Kronberg, and H. Böhringer, Astrophys. J. Lett. 547 (2001) L111; J.-L. Han and R. Wielebinski, Chinese Journal of Astronomy and Astrophysics 2 (2002) 293 `astro-ph/0209090`; P. P. Kronberg, Physics Today 55, December 2002, p. 40.

[27] Y. Xu, P. P. Kronberg, S. Habib and Q. W. Dufton, `astro-ph/0509826`.

[28] M. V. Medvedev, L. O. Silva and M. Kamionkowski, `astro-ph/0512079`.

[29] D. Ryu, H. Kang, and P. L. Biermann, Astron. Astrophys. **335** (1998) 19.

[30] F. Miniati, Mon. Not. Roy. Astron. Soc. **337**, 199 (2002) `astro-ph/0203014`.

[31] `http://www.grinninglizard.com/tinyxml/`

[32] `http://heasarc.gsfc.nasa.gov/docs/software/fitsio`

[33] `http://www.cern.ch/clhep/`